COMMUNICATION

Check for updates

A facile strategy for the large-scale preparation of starch-based AIE luminescent nanoaggregates *via* host–guest interactions and their versatile applications†

Yupeng Shi,[ab] Yaning Xia,[b] Mengyang Zhou,[b] Qiuna Shi,[c] Li Meng,[c] Chuen Kam,[a] Hui Gao, [iD][a] Jingliang Cheng, [iD][b] Ben Zhong Tang, [iD][de] Sijie Chen [iD] *[af] and Engui Zhao [iD] *[g]

Luminescent nanomaterials with outstanding optical properties have attracted growing interest due to their widespread applications. However, large-scale fabrication of luminescent nanomaterials with desired properties through a simple and economical process remains challenging. As a renewable natural resource, starch is non-toxic, easily accessible, and inexpensive, making it a popular choice for uses in various biomedical fields. In this work, we present a facile assembly strategy for the fabrication of starch-based luminescent nanoaggregates using starch as the host material and aggregation-induced emission luminogens (AIEgens) as guest molecules. By employing simple procedures under mild conditions, highly luminescent nanoparticles with small sizes, high water dispersibility, and low cytotoxicity are prepared on a large scale. The resulting nano-assemblies demonstrate significantly enhanced fluorescence intensities, reduced susceptibility to photobleaching and low cytotoxicity. These fluorescent supramolecular aggregates can be employed in various application fields, including the fabrication of fluorescent hydrogels, fingerprint detection, cell imaging and *in vivo* lymphatic system imaging. The methodology developed in this work has immense potential to greatly promote the production of high-quality nanoparticles on the industrial scale, offering a cost-effective solution that can meet the needs of various applications and pave the way for wider implementation of nanotechnology.

New concepts

This work demonstrates a simple and effective manufacturing strategy for fluorescent nanomaterials by employing starch as the host. This method utilized the cavity structure of starch and the host–guest interactions between aggregation-induced luminescent dyes to quickly and extensively generate luminescent nanoparticles. It is worth noting that this manufacturing method is not only suitable for hydrophobic fluorescent dyes but also works well for hydrophilic fluorescent dyes. These fluorescent nanoaggregates demonstrated good biocompatibility and anti-photobleaching properties, enabling them to be widely used in fluorescent hydrogel manufacturing, fingerprint detection, and biological imaging. Therefore, this work may open up a universal pathway for the rapid preparation of novel fluorescent nanomaterials and pave the way for exploring their practical applications.

[a] Ming Wai Lau Centre for Reparative Medicine, Karolinska Institutet, Hong Kong 999077, China. E-mail: sijie.chen@ki.se

[b] Department of Magnetic Resonance Imaging, The First Affiliated Hospital of Zhengzhou University, Zhengzhou 450052, China

[c] Department of Criminal Science and Technology, Henan Police College, Zhengzhou 450046, China

[d] Department of Chemistry, The Hong Kong University of Science and Technology, Clear Water Bay, Kowloon, Hong Kong 999077, China

[e] School of Science and Engineering, Shenzhen Institute of Aggregate Science and Technology, The Chinese University of Hong Kong, Shenzhen (CUHK-Shenzhen), Guangdong 518172, China

[f] School of Life Sciences, The Chinese University of Hong Kong, Shatin, New Territories, Hong Kong 999077, China

[g] School of Science, Harbin Institute of Technology, Shenzhen, HIT Campus of University Town, Shenzhen 518055, China. E-mail: zhaoengui@hit.edu.cn

† Electronic supplementary information (ESI) available. See DOI: https://doi.org/10.1039/d3mh01717f

Introduction

Fluorescent dyes with high quantum yields, good photostability, and excellent biocompatibility are advantageous in practical applications.[1–6] However, most fluorescent dyes suffer from poor photostability, easy photobleaching, short fluorescence lifetimes, and considerable biological toxicity.[7–9] The packaging, modification, or assembly of these fluorescent dyes into nanomaterials can solve the aforementioned problems, greatly expanding their application potential in biological imaging, chemical sensing, and optoelectronics.[10–13] Nevertheless, conventional fluorophores with strong intermolecular π–π stacking and hydrophobic interactions experience fluorescence quenching at high concentrations and in the aggregated state, which restricts their applications at high concentrations and in the aggregated state.[14–17] Therefore, scientists have consistently pursued fluorescent dyes with high aggregate-state luminescence.
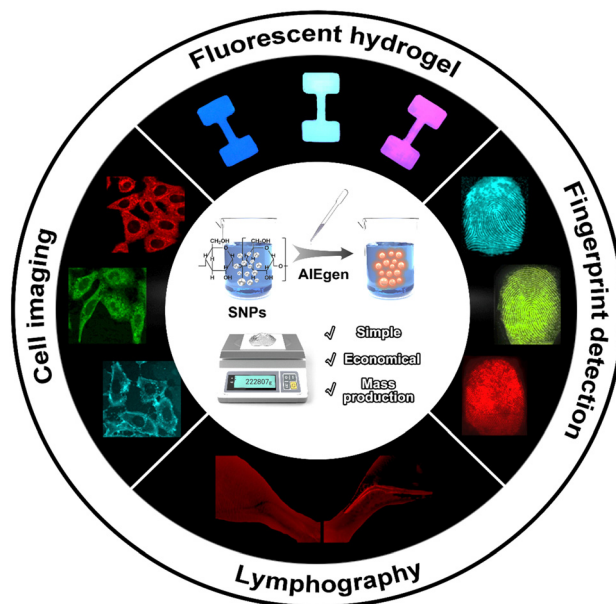
In 2001, a class of fluorescent materials with aggregation-induced emission (AIE) characteristics was reported, and this discovery has been attracting increasing attention.[18–21] AIE luminogens (AIEgens) are almost non-emissive when dissolved

in dilute solutions but they become highly emissive in the solid or aggregated state. Systematic investigations have revealed that restriction of intramolecular motions and a highly distorted molecular conformation account for this phenomenon.[22] Many AIE-active fluorescent dyes with varying degrees of hydrophilicity have been prepared and employed in various application fields. By taking advantage of the AIE effect, AIEgens were also used in the fabrication of high-performance fluorescent nanomaterials.[19] Upon integration into the nanomaterials, the AIEgens were placed in confined environments with restricted intramolecular motions, which significantly promoted the fluorescence decay of these AIEgens. At present, various strategies, such as functionalization in a rigid metal–organic framework (MOF) through coordination polymerization, bonding to the inner surface of mesoporous silica nanoparticles, and absorption onto biopolymers, have been developed to construct AIEgen-based hybrid nanomaterials.[23,24] However, it remains challenging to develop a universal method for effectively applying these AIEgens in practical applications.

Macrocycles, including cyclodextrins, cucurbiturils, calixarenes, and pillararenes, serve as supramolecular hosts capable of enveloping guest molecules in their inner cavities to form fluorescent inclusion complexes.[25–28] Their inner cavities could provide feasible platforms to reduce the intramolecular motions of fluorescent materials through non-covalent interactions. In addition, constructing nanomaterials through host–guest interactions works well for both hydrophilic and hydrophobic fluorescent dyes, which have been employed in multiple fields, such as fluorescence imaging, fingerprint recognition, and chemical sensing.[29–32]

As a natural, renewable, and biodegradable macromolecular polysaccharide, starch has the advantages of good biocompatibility, non-immunogenicity, excellent stability in the air, abundance, and low cost, making it an attractive food, pharmaceutical, and chemical raw material. In addition, starch with α-D-glucose chains possesses a large number of external hydroxyl groups, forming a spiral structure. This spiral structure allows for the inclusion of various functional substances, including iodine ions, metal ions and organic dyes,[33–35] and thus imparts many interesting attributes to the starch host. Therefore, it is a desirable compound for constructing functional fluorescent materials,[36–39] which have demonstrated great potential in biomedical applications.[40–42] In this work, we report a simple and efficient strategy for the fabrication of fluorescent nanomaterials. By taking advantage of the host–guest interactions with starch, both hydrophobic and hydrophilic AIEgens could be facilely fabricated into luminescent nanoparticles on a large scale and at low cost. These as-prepared fluorescent nanoaggregates exhibit good biocompatibility and anti-photobleaching attributes, making them suitable for versatile applications in fluorescent hydrogel fabrication, fingerprint detection, and bioimaging (Scheme 1). This work may open up a universal avenue for the fabrication of novel fluorescent nanoaggregates and pave the way for the exploration of their practical applications.

Scheme 1 The fabrication processes and versatile applications of starch-based luminescent nanomaterials in this work.

Results and discussion

Synthesis of starch nanoparticles (SNPs)

SNPs were obtained by a simple ultrasonic-assisted acid hydrolysis method which can overcome the shortcomings of a single synthesis method, such as long time and low yields[43] (Fig. 1a). Corn starch granules were used as raw materials to prepare starch nanomaterials, and their surface morphologies were examined by scanning electron microscopy (SEM). As shown in Fig. S1 (ESI†), starch granules appeared as oval and irregular
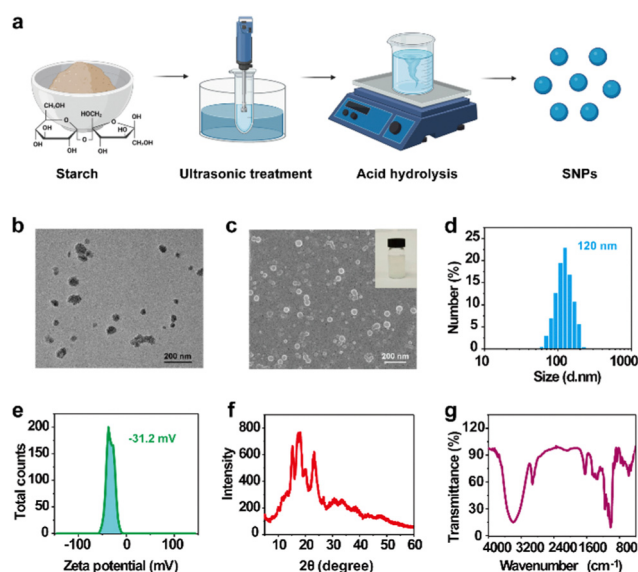

Fig. 1 (a) Schematic diagram of the formation of starch nanoparticles. (b)–(g) Characterization of the morphology and properties of starch nanoparticles by employing (b) TEM, (c) SEM, (d) DLS, (e) zeta potential, (f) XRD, and (g) FTIR techniques.

polygons with smooth surfaces, exhibiting a wide range of particle sizes ranging from 3 to 30 μm. Then, SNPs were prepared by ultrasonic-assisted acid hydrolysis with a yield of ~24.5 wt%, which was much higher than that achieved by single acid hydrolysis.[44] The obtained SNPs exhibited an irregular round structure with a particle size of ~80 nm and could be stably dispersed in aqueous solution (Fig. 1b), showing the classical Tyndall effect. Besides, slight aggregation (Fig. 1c) was observed in the SEM images of these SNPs, which was due to the destruction of extensive amorphous areas caused by hydrolysis and the subsequent aggregation of crystalline components during drying. The SNPs were then subjected to dynamic light scattering (DLS) characterization studies, revealing a relatively wide particle size distribution with an average particle size of ~120 nm (Fig. 1d). The average particle size was slightly larger than that observed by transmission electron microscopy (TEM), presumably due to the presence of a hydrate layer of sugar hydroxyl groups on the surface of SNPs in solutions.[33] Additionally, the measured surface zeta potential of SNPs was −31.2 mV (Fig. 1e), which was consistent with their high stability in solutions.

Then, the crystallization properties of SNPs were studied by X-ray diffraction (XRD). As shown in Fig. 1f, the SNPs showed a typical A-mode diffraction pattern with significant diffraction peaks at 2θ of 15.3°, 17.3°, 18.1° and 23.2°. SNPs prepared by the ultrasonic-assisted acid-hydrolysis method retained the crystal form of natural starch to the greatest extent. As acid hydrolysis mainly destroyed the amorphous region of starch, the relative crystallinity (RC) of SNPs was ~46.5%, which was higher than the reported crystallinity of natural starch. Fourier transform infrared spectroscopy (FTIR) was used to characterize the functional groups and molecular structures of SNPs. As shown in Fig. 1g, the strong absorption band near 3403 cm^{-1} was attributed to the stretching of hydrogen-bonded hydroxyl groups of starch. The band at 2925 cm^{-1} was characteristic of C–H stretching associated with the hydrogen atom SNP of –CH$_3$ and –CH$_2$. The peak near 1637 cm^{-1} originated from the O-H bending vibration of water tightly bound in starch. The peaks ranging from 1334 cm^{-1} to 1458 cm^{-1} corresponded to the absorption peaks of C–H bending vibration in the glucose unit, while 1160 cm^{-1} represented the absorption peak of hydroxyl stretching vibration in secondary alcohol. The characteristic peak at 1022 cm^{-1} was attributed to the tensile vibration of the starch hydroxyl group. All these results fully demonstrated the successful preparation of SNPs.

Characterization studies on fluorescent SNPs

The fluorescence enhancement of AIEgens by SNPs was investigated through photoluminescence spectrometry. AIEgens with different sizes and charges were dissolved in water at low concentrations without obvious fluorescence (Fig. S2, ESI†). Upon the addition of SNPs, the fluorescence intensities of the systems were significantly enhanced, which could be visually observed under the irradiation of a handheld UV lamp (Fig. S2, ESI†, insets). In trial experiments, we found that AIEgens with positively charged groups or a certain degree of linear structures

showed more pronounced fluorescence enhancement than others. Considering the electronegativity and the spiral cavity structure of SNPs, we hypothesized that the fluorescence enhancement possibly resulted from the entry of the entire or part of AIEgens into the spiral cavity of starch through host–guest interactions, which in turn restricted the motions of AIEgens and led to a significant fluorescence enhancement (Fig. 2a). Therefore, we used SNPs doped with three different fluorescent AIEgens, namely, B, Y, and R, respectively, to study this phenomenon and its possible mechanism.

B, Y, and R possessed positive charges or linear structures (Fig. S3, ESI†). The solutions of these AIEgens were homogeneous at low concentrations, which turned to uniform emulsions (hereafter named as SNP-B, SNP-Y, and SNP-R, respectively) with white, green, and yellow appearance, respectively, after addition of SNPs (Fig. S4, ESI†). Fluorescence enhancements were observed with slight blueshifts after adding SNPs into the solutions of B, Y, and R (Fig. 2b), which was accompanied by an increase in the fluorescence quantum yields of these solutions from 0.015, 0.005, and 0.017 to 0.03, 0.147, and 0.218, respectively (Table S1, ESI†). The uniform distributions of the concentrated nanocomposites in the centrifuged pellets suggested the strong affinity between B/Y/R and SNPs (Fig. S5, ESI†). The resulting precipitates were then collected and dried. White powders of SNPs (Fig. S6, ESI†) were endowed with pale yellow to brown
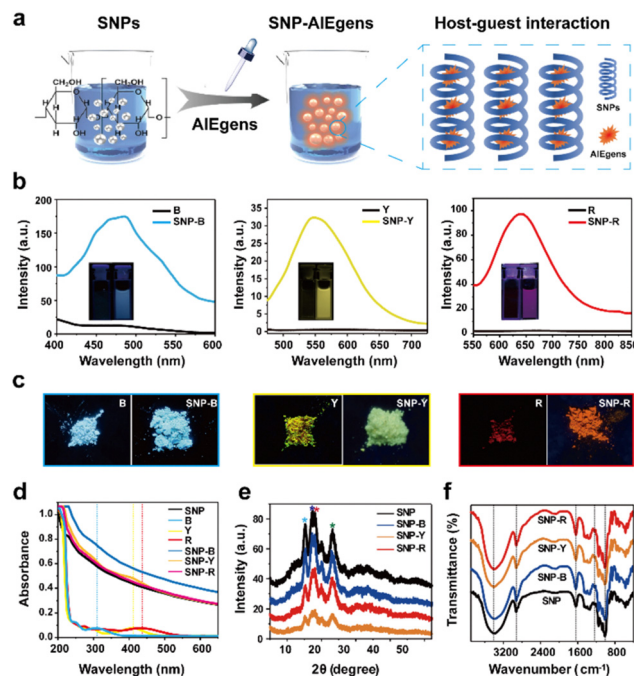

Fig. 2 (a) Schematic diagram of the formation of the fluorescence nanoaggregates. (b) The fluorescence spectra and fluorescence images of B, SNP-B, Y, SNP-Y, R, and SNP-R in 1 μM aqueous solutions. For SNP-B, SNP-Y and SNP-R, 8 mg of SNPs was added to 1 mL dye aqueous solutions (1 μM). (c) Fluorescence photographs of B, Y, R, SNP-B, SNP-Y, and SNP-R powders upon irradiation with a 365 nm UV lamp. (d) UV-vis absorption spectra of SNP, B, SNP-B, Y, SNP-Y, R, and SNP-R in aqueous solutions. (e) XRD spectra of SNP, SNP-B, SNP-Y, and SNP-R. (f) FTIR spectra of SNP, SNP-B, SNP-Y, and SNP-R.

colors in SNP-B, SNP-Y, and SNP-R powders after the inclusion of AIEgens (Fig. S7, ESI†). Solid SNPs exhibited very weak fluorescence under UV irradiation at 365 nm, while SNP-B, SNP-Y, and SNP-R showed strong blue, yellow and red fluorescence, respectively (Fig. 2c). The fluorescence quantum yields of SNP-B, SNP-Y, and SNP-R in the solid state were 0.732, 0.373, and 0.103, respectively, which were much higher than those of B, Y, and R with fluorescence quantum yields of 0.536, 0.065, and 0.024, respectively (Table S1, ESI†).

To explore the structural evolutions of SNPs upon combination with B/Y/R, we compared their SEM, UV-vis, XRD, and FTIR results. There were no obvious changes in the morphology of SNPs with respect to SNP-B, SNP-Y, and SNP-R (Fig. S8, ESI†). UV-vis spectra illustrated that B/Y/R were efficiently bound to SNPs (Fig. 2d). XRD results indicated that the crystallinities of SNP-B/Y/R were decreased slightly, which was possibly due to a slight change in SNP conformations upon the insertion of AIEgens (Fig. 2e). The FTIR spectra of SNP-B/Y/R showed no obvious difference compared to that of SNPs (Fig. 2f). This was because the tiny amounts of AIEgens added did not influence the core structure of SNPs significantly. The above data showed that new fluorescent starch-AIE nanomaterials were obtained through facile strategies. It should be noted that this manufacturing method not only increased the local aggregation concentrations of AIEgens to enhance their fluorescence intensity, but also used simple raw materials to enable large-scale production of fluorescent nanomaterials, which was of great significance in improving their performance and applicability.

SNP-enhanced fluorescence of AIEgens

To achieve the optimal ratios of SNPs and B/Y/R in forming nanoaggregates, we added different amounts of SNPs to B/Y/R solutions. With the continuous addition of SNPs, B/Y/R entered the spiral cavity of SNPs or adsorbed on the surface to form well dispersed nanocomposites, and the corresponding fluorescence intensities were gradually increased (Fig. 3a–c). Natural light transmission indicated that the optical transparency of

the system was decreased (Fig. S9, ESI†). As the amount of starch was further increased, fewer free B/Y/R molecules were available to bind SNPs, and the fluorescence intensities of the solutions reached plateaus (Fig. 3d–f). These results indicated that the starch surface had strong interactions with B/Y/R, which restricted the intramolecular movements of B/Y/R and enhanced their emissions.

Host–guest interaction mechanism

Although SNPs could effectively enhance the fluorescence intensity of water-soluble AIEgens, its underlying mechanism was still elusive. Therefore, we tested whether monosaccharides or oligosaccharides could enhance the fluorescence of B/Y/R solutions. As shown in Fig. 4a–c, the fluorescence intensities of B/Y/R solutions were not increased significantly in the presence of monosaccharides (glucose) or oligoglucans (dextran). Although the addition of dextran increased the fluorescence intensities of B/Y/R solutions to a certain extent, this was mainly due to the increase in solution viscosity, which could also restrict the intramolecular motions of AIEgens. Starch is well known for its special hydrophobic cavity in the single helix, which could accommodate small molecules, such as iodine, while monosaccharides and oligosaccharides do not possess this tertiary structure.

To confirm the critical role of the spatial structure of starch in accommodating B/Y/R, iodine was added into the starch solution as a competitor of B/Y/R. For all three AIEgens, iodine reduced the fluorescence intensity of SNP-B/Y/R to a certain extent (Fig. 4d–f), but this phenomenon was not observed in DSPE-PEG$_{2000}$-B/Y/R (Fig. S10, ESI†). Therefore, the stable starch–iodine complex reduced starch cavities to B/Y/R, which led to a decrease in the fluorescence of B/Y/R. The results
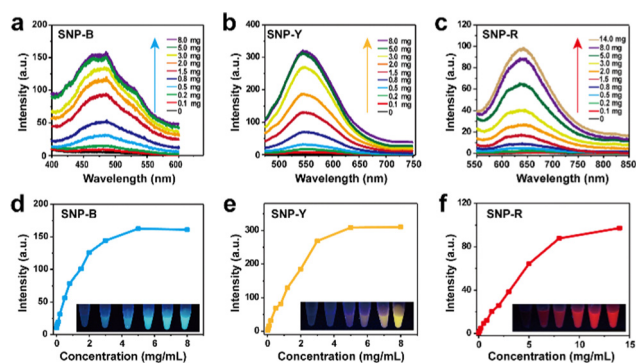

Fig. 3 (a)–(c) Fluorescence responses of 1 μM dye solution in 1 mL H$_2$O solution upon addition of 0 to 14 mg SNPs. a.u., arbitrary unit. (d)–(f) Plots of fluorescence intensity of the dye solutions as a function of the SNP concentrations. Insets show the fluorescence images of 1 μM dye with different concentrations of SNPs (0, 0.1, 0.5, 1.5, 3.0, and 8.0 mg mL^{-1}) taken under a 365 nm handheld UV lamp. a.u., arbitrary unit.
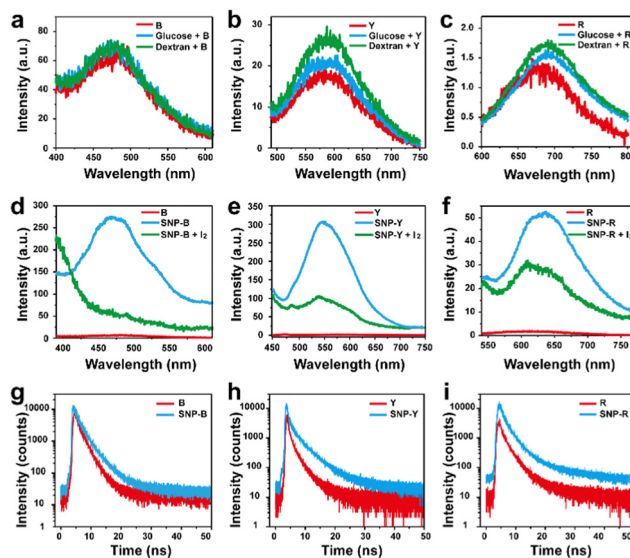

Fig. 4 (a)–(c) Fluorescence spectra of B/Y/R, glucose + B/Y/R, and dextran + B/Y/R. a.u., arbitrary unit. (d)–(f) Fluorescence spectra of B/Y/R, SNP-B/Y/R, and SNP-B/Y/R + I$_2$. a.u., arbitrary unit. (AIEgen: 1 μM; SNPs, glucose, dextran: 8.0 mg mL^{-1}, and I$_2$:1.0 mg mL^{-1}) Fluorescence decay curves of (g) B, SNP-B; (h) Y, SNP-Y; and (i) R, SNP-R.

suggested that B/Y/R could enter the spiral cavities of SNPs, which restricted their intramolecular motions and enhanced their fluorescence. The fluorescence lifetime usually depends on the microenvironment of luminogens. Compared with B/Y/R, SNP-B/Y/R had longer fluorescence lifetimes (Fig. 4g–i). Therefore, restricted intramolecular motions of B/Y/R in starch cavities promoted excited-state electrons to return to the ground state through radiative decay pathways.

Properties of starch luminescent nanoaggregates (SLNs)

Many AIEgens are featured with poor water solubilities and high biological toxicities, so they are often decorated with 1,2-distearoyl-sn-glycero-3-phosphoethanolamine-polyethylene glycol-2000 (DSPE-PEG$_{2000}$) for better dispersion in aqueous media and improved performances. At the same B/Y concentrations, the fluorescence intensities of SNP-B and SNP-Y were higher than those of DSPE-PEG$_{2000}$-B and DSPE-PEG$_{2000}$-Y, respectively, while SNP-R was not as bright as DSPE-PEG$_{2000}$-R (Fig. S11, ESI†). This indicated the stronger interactions between DSPE-PEG$_{2000}$ and R. We further compared the photostability of B/Y/R, SNP-B/Y/R, and DSPE-PEG$_{2000}$-B/Y/R by irradiating their solutions in a UV light box. Within 100 min of irradiation, all B/Y/R solutions exhibited more than 70% fluorescence attenuations (Fig. 5a–c). Among the DSPE-PEG$_{2000}$-decorated nanoparticles, DSPE-PEG$_{2000}$-B experienced the most significant fluorescence attenuation, while DSPE-PEG$_{2000}$-R showed almost none. Intriguingly, the photobleaching of SNP-B/Y/R was all less than 20% under the same conditions, which was much slower compared to the control groups.

To evaluate the biocompatibility of nanoaggregates, the cytotoxicity of SNPs was determined in HeLa, NIH/3T3 and 4T1 cells using CCK-8 assay. SNPs exerted no obvious cytotoxicity on HeLa and NIH/3T3 cells (Fig. 5d–f and Fig. S12, ESI†). Compared with B/Y/R, SNP-B/Y/R showed higher cell viability in all the groups (Fig. 5d–f), suggesting that SNPs could effectively reduce the cytotoxicity of B/Y/R. This may be mainly attributed to the host–guest interaction between fluorescent dyes and starch, which can effectively reduce the direct interaction between AIEgens and cells, thereby greatly alleviating their damage to cells. In order to determine the antioxidant properties of SNP-B/Y/R, 2′,7′-dichlorodihydrofluorescein diacetate (DCFH-DA), a free-radical-reactive dye, was used to detect ROS levels. Compared to B/Y/R, SNP-B/Y/R produced less ROS in cells under irradiation, and the differences were more significant when the irradiated cells were placed in dark for 15 h (Fig. 5g). Live-cell fluorescence imaging of DCFH-DA also showed that SNP-R generated less ROS in cells after irradiation than R (Fig. 5h). These data suggested that SNP decoration reduced the cytotoxicity of AIEgens and widened their potential in biological applications.

Versatile applications of SLNs

Fluorescent polymer hydrogels, which are three-dimensional cross-linked hydrophilic polymer networks with tunable luminescence properties, are an emerging class of luminescent materials for luminescence sensing, display, and information
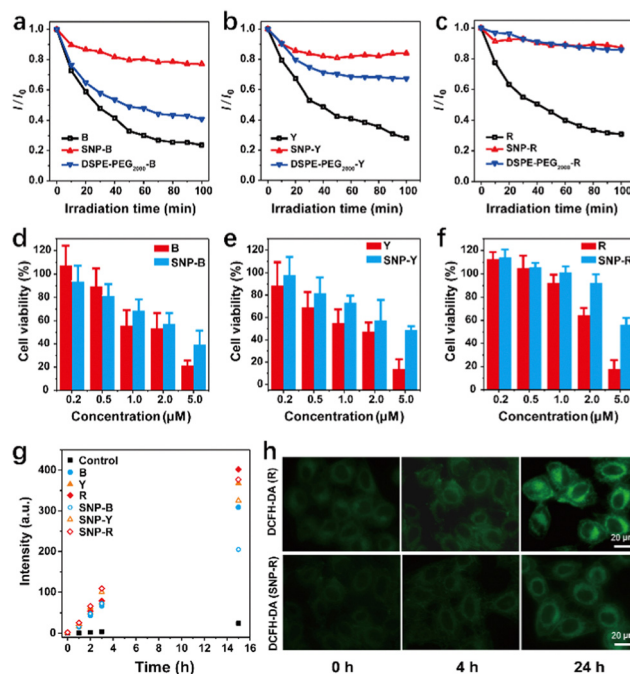
Fig. 5 (a)–(c) Photostability of B/Y/R, DSPE-PEG$_{2000}$-B/Y/R, and SNP-B/Y/R irradiated with 365 nm UV light for 100 min under ambient conditions. I_0, the initial intensity; I, the fluorescence intensity at designated time. (AIEgens: 1 μM; SNPs: 8.0 mg mL^{-1}) (d)–(f) cytotoxicity of B, SNP-B, Y, SNP-Y, R, and SNP-R on 4T1 cells after 24 h of incubation. Data represent mean ± standard deviation. n = 6 independent experiments. (g) Evaluation of ROS generation in HeLa cells using a plate reader. After incubation with 10 μM B/Y/R or SNP-B/Y/R for 4 h, 150 μL of DCFH-DA solutions was added to each well, followed by irradiating the cells with white light (0.22 W cm^{-2}) for 5 min. The fluorescence intensities at 488 nm were examined at the designated time. a.u., arbitrary unit. (h) Fluorescence images of HeLa cells incubated with DCFH-DA to assess the ROS level after incubation with R or SNP-R.

encryption. To test whether SLNs improved the properties of AIEgen-doped hydrogels (Fig. S13, ESI†), we compared the fluorescence intensity of hydrogels doped with B/Y/R and SNP-B/Y/R. The hydrogels doped with B/Y/R exhibited very weak fluorescence, whereas the hydrogels doped with SNP-B/Y/R showed an obvious increase in fluorescence intensity (Fig. 6a and b). Moreover, the fluorescence became stronger as SNP concentrations were increased.

Latent fingerprints (LFPs) are formed by biogenic substances secreted by sweat glands when fingers come into contact with objects. LFP, which is almost invisible to the naked eye, is the most common fingerprint type at the crime scene. Therefore, LFP development is crucial for forensic science. The feasibility of using SLN powders to visualize LFP on different object surfaces, including paper, glass, and plastic, was investigated. Under normal circumstances, these imprints could not be recognized by the naked eye (Fig. 6c). While under UV excitation, LFP could be clearly seen by collecting fingerprints on the surfaces of different materials with a fingerprint brush. These results indicated the versatility and effectiveness of our newly developed SLN powders. Besides, the feasibility of employing SLNs in fluorescence live-cell imaging was also
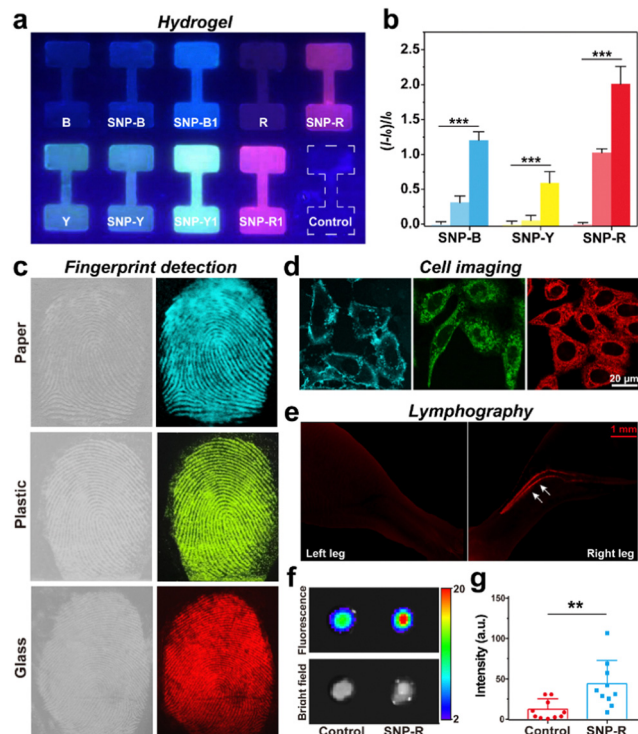
Fig. 6 (a) Fluorescence images of hydrogels doped with different fluorescent materials. B, Y and R were doped with 1 µM of B, Y and R, respectively, while B1, Y1, and R1 were doped with 2 µM of B, Y and R, respectively. (b) Quantitative analysis of relative fluorescence intensities of fluorescence hydrogels. Data represent mean $\pm$ standard deviation. $n = 3$, ***$P < 0.001$. I_0, the initial intensity of B, Y or R group; I, the measured intensity in the designated group. (c) Fingerprint detection on paper, plastic, and glass with SNP-B, SNP-Y, or SNP-R. (d) Fluorescence imaging of 4T1 cells with SNP-B, SNP-Y, or SNP-R at AIEgen concentrations of 10 µM. (e) *In vivo* imaging of lymphatic vessels in mouse legs after injection of R (left) and SNP-R (right). (f) Heatmap of fluorescence signals in lymph nodes of mice 30 min after intradermal injection of SNP-R (4 mg mL^{-1}) into the hind paw. (g) Quantitative analysis of fluorescence intensity at bilateral lymph node sites. Data represent mean $\pm$ standard deviation. $n = 3$, **$P < 0.01$. a.u., arbitrary unit.

explored. Upon 488 nm excitation, HeLa cells incubated with SNP-B/Y/R showed fluorescence signals in the range of 500–550 nm (Fig. 6d). Notably, enhanced fluorescence was observed in SNP-B/Y/R-treated HeLa cells. As a result, HeLa cells incubated with SNP-B/Y/R could be directly imaged without obvious background fluorescence even without the washing step, presumably due to the high cell uptake of these materials. Moreover, SNP-B/Y/R were also applicable to intracellular imaging of several other cell lines, which demonstrated their great potentials in cell imaging (Fig. S14, ESI†). To further investigate whether SLNs were applicable to *in vivo* fluorescence imaging, fluorescence images were collected immediately after injecting SNP-R into the footpad of the mice. As shown in Fig. 6e, the red fluorescence signals of nanoparticles in lymphatic vessels and lymph nodes were clearly detected, and a distinct lymphatic vessel contour was observed (arrow position). In contrast, only weak fluorescence signals were observed in the lymph nodes injected with R solution. Furthermore, *ex vivo*

fluorescence imaging of the resected lymph nodes was conducted immediately after injection. Strong fluorescence signals were observed in the lymph nodes, which were consistent with the imaging results (Fig. 6f). Region of interest measurements showed that the signal-to-background ratio in lymph nodes was 10 for R and 40 for SNP-R. (Fig. 6g). This result illustrated that SNPs enhanced the fluorescence performance of AIEgens in *in vivo* imaging.

Conclusions

In this work, a facile, low-cost, and mass-construction strategy was developed for the preparation of brightly emissive multicolor SLNs. The synthesized composite nanomaterials possessed small sizes, excellent water dispersibility, and biocompatibility. Notably, this strategy significantly enhanced the fluorescence quantum yields of AIEgens through the host–guest interactions between the starch and the AIEgens, and the SLNs exhibited lower intracellular cytotoxicity and higher photostability compared to the corresponding pure AIEgens. The SLNs can be adsorbed by hydrogels to construct fluorescent hydrogels, which can be further applied in information encoding. Latent fingerprints on various surfaces can be visualized using the SLN powders. We also demonstrated the feasibility of employing these SLNs for multicolor cell imaging and *in vivo* imaging of the lymphatic system. This strategy, suitable for cost-effective and scalable production of high-quality nanoparticles, offers a promising outlook for the widespread applications of nanomaterials and facilitates the growth of the nanotechnology industry.

Author contributions

Yupeng Shi, Yaning Xia, and Mengyang Zhou designed and conducted the experiments, and wrote the original draft; Qiuna Shi, Li Meng wrote and reviewed the manuscript, and administrated the project; Chuen Kam and Hui Gao curated the data; Jingliang Cheng provided technical support; Ben Zhong Tang supervised the project and reviewed and edited the manuscript; Sijie Chen and Engui Zhao supervised the project, acquired funds and wrote, reviewed and edited the manuscript.

Conflicts of interest

There are no conflicts of interest to declare.

Acknowledgements

Notes and references

1 G. Gupta, P. Kumari, J. Y. Ryu, J. Lee, S. M. Mobin and C. Y. Lee, *Inorg. Chem.*, 2019, **58**, 8587–8595.

2 A. R. Nodling, E. M. Mills, X. F. Li, D. Cardella, E. J. Sayers, S. H. Wu, A. T. Jones, L. Y. P. Luk and Y. H. Tsai, *Chem. Commun.*, 2020, **56**, 4672–4675.

3 Y. Pan, Y. P. Shi, J. Y. Chen, C. M. Wong, H. Zhang, M. J. Li, C. W. Li and C. Q. Yi, *Mater. Sci. Eng., C*, 2016, **69**, 561–568.

4 Z. Shi, X. Han, W. Hu, H. Bai, B. Peng, L. Ji, Q. Fan, L. Li and W. Huang, *Chem. Soc. Rev.*, 2020, **49**, 7533–7567.

5 L. L. Wang, W. Du, Z. J. Hu, K. Uvdal, L. Li and W. Huang, *Angew. Chem., Int. Ed.*, 2019, **58**, 14026–14043.

6 J. Zhang, X. Chai, X.-P. He, H.-J. Kim, J. Yoon and H. Tian, *Chem. Soc. Rev.*, 2019, **48**, 683–722.

7 C. Duan, M. Won, P. Verwilst, J. Xu, H. S. Kim, L. Zeng and J. S. Kim, *Anal. Chem.*, 2019, **91**, 4172–4178.

8 F. Deng and Z. Xu, *Chin. Chem. Lett.*, 2019, **30**, 1667–1681.

9 U. Resch-Genger, M. Grabolle, S. Cavaliere-Jaricot, R. Nitschke and T. Nann, *Nat. Methods*, 2008, **5**, 763–775.

10 Y. Shi, C. Yi, Z. Zhang, H. Zhang, M. Li, M. Yang and Q. Jiang, *ACS Appl. Mater. Interfaces*, 2013, **5**, 6494–6501.

11 K. Zhang, Y.-J. Gao, P.-P. Yang, G.-B. Qi, J.-P. Zhang, L. Wang and H. Wang, *Adv. Healthcare Mater.*, 2018, **7**, 1800344.

12 Y. Zhang, F. Fang, L. Li and J. Zhang, *ACS Biomater. Sci. Eng.*, 2020, **6**, 4816–4833.

13 H. Chen, K. Shou, S. Chen, C. Qu, Z. Wang, L. Jiang, M. Zhu, B. Ding, K. Qian, A. Ji, H. Lou, L. Tong, A. Hsu, Y. Wang, D. W. Felsher, Z. Hu, J. Tian and Z. Cheng, *Adv. Mater.*, 2021, **33**, 2006902.

14 Y. Huang, J. Xing, Q. Gong, L.-C. Chen, G. Liu, C. Yao, Z. Wang, H.-L. Zhang, Z. Chen and Q. Zhang, *Nat. Commun.*, 2019, **10**, 169.

15 S. Wang, Y. Fan, D. Li, C. Sun, Z. Lei, L. Lu, T. Wang and F. Zhang, *Nat. Commun.*, 2019, **10**, 48.

16 M. Zhang, J. Chen, M. Wang, M. Yuan, R. Li, X. Feng, Y. He, X. Mao, Y. Li, Z. Xiong, Z. Xing, J. Hu and G. Wu, *ACS Appl. Mater. Interfaces*, 2021, **13**, 9036–9042.

17 C. Ou, C. An, Z. Zhao, F. Gao, L. Zheng, C. Xu, K. Zhang, J. Shao, L. Xie and X. Dong, *Aggregate*, 2023, **4**, e290.

18 S. Chen, H. Wang, Y. Hong and B. Z. Tang, *Mater. Horiz.*, 2016, **3**, 283–293.

19 H. Gao, X. Zhao and S. Chen, *Molecules*, 2018, **23**, 419.

20 E. Zhao and S. Chen, *Mater. Chem. Front.*, 2021, **5**, 3322–3343.

21 M.-Y. Wu, J.-K. Leung, C. Kam, T. Y. Chou, J.-L. Wang, X. Zhao, S. Feng and S. Chen, *Sci. China: Chem.*, 2022, **65**, 979–988.

22 H. Zhang, Z. Zhao, A. T. Turley, L. Wang, P. R. McGonigal, Y. Tu, Y. Li, Z. Wang, R. T. K. Kwok, J. W. Y. Lam and B. Z. Tang, *Adv. Mater.*, 2020, **32**, 2001457.

23 Y. Wang, M. Chen, N. Alifu, S. Li, W. Qin, A. Qin, B. Z. Tang and J. Qian, *ACS Nano*, 2017, **11**(10), 10452–10461.

24 X. Cai and B. Liu, *Angew. Chem., Int. Ed.*, 2020, **59**, 9868–9886.

25 D. Li and J. Yu, *Small*, 2016, **12**, 6478–6494.

26 X. Huang, M. Lan, J. Wang, L. Guo, Z. Lin, N. Sun, C. Wu and B. Qiu, *Biosens. Bioelectron.*, 2020, **169**, 112655.

27 X. Du, H. Hao, A. Qin and B. Z. Tang, *Dyes Pigm.*, 2020, 180.

28 C. Chen, X. Ni, H.-W. Tian, Q. Liu, D.-S. Guo and D. Ding, *Angew. Chem., Int. Ed.*, 2020, **59**, 10008–10012.

29 Y.-Y. Chen, X.-M. Jiang, G.-F. Gong, H. Yao, Y.-M. Zhang, T.-B. Wei and Q. Lin, *Chem. Commun.*, 2021, **57**, 284–301.

30 X.-Y. Lou and Y.-W. Yang, *Aggregate*, 2020, **1**, 19–30.

31 J.-S. Shen, D.-H. Li, Y.-B. Ruan, S.-Y. Xu, T. Yu, H.-W. Zhang and Y.-B. Jiang, *Luminescence*, 2012, **27**, 317–327.

32 I. Helmers, M. Saddam Hossain, N. Baumer, P. Wesarg, B. Soberats, L. S. Shimizu and G. Fernandez, *Angew. Chem., Int. Ed.*, 2022, **61**, e202200390.

33 X.-H. Wang, X.-Y. Lou, T. Lu, C. Wang, J. Tang, F. Liu, Y. Wang and Y.-W. Yang, *ACS Appl. Mater. Interfaces*, 2021, **13**, 4593–4604.

34 H.-Y. Kim, S. S. Park and S.-T. Lim, *Colloids Surf., B*, 2015, **126**, 607–620.

35 J. Kaur, G. Kaur and S. Sharma, *Acta Aliment.*, 2019, **48**, 204–212.

36 H. Gujral, A. Sinhmar, M. Nehra, V. Nain, R. Thory, A. K. Pathera and P. Chavan, *Int. J. Biol. Macromol.*, 2021, **186**, 155–162.

37 Y. Wang, J. Nie, W. Fang, L. Yang, Q. Hu, Z. Wang, J. Z. Sun and B. Z. Tang, *Chem. Rev.*, 2020, **120**, 4534–4577.

38 S. Wang, J. Zhan, Z. Jin and Y. Tian, *Food Hydrocolloids*, 2017, **63**, 286–292.

39 Y. Li, Y. Tan, Z. Ning, S. Sun, Y. Gao and P. Wang, *Carbohydr. Polym.*, 2011, **86**, 291–295.

40 F. Song, C. Zhang, H. Dong, Y. Fan, M.-Y. Wu, G. Shan, P. Lai, H. Gao and Y. S. Zhao, *J. Mater. Chem. C*, 2021, **9**, 11180–11188.

41 S. F. Chin, A. Azman, S. C. Pang and S. M. Ng, *J. Nanomater.*, 2014, **2014**, 108359.

42 M. Liu, H. Huang, K. Wang, D. Xu, Q. Wan, J. Tian, Q. Huang, F. Deng, X. Zhang and Y. Wei, *Carbohydr. Polym.*, 2016, **142**, 38–44.

43 Y. Xue, M. Liu, H. Huang, F. Deng, G. Zeng, Q. Wan, S. Liang, X. Zhang and Y. Wei, *RSC Adv.*, 2016, **6**, 76011–76016.

44 Y. Dong, W. Wang, C. Zhong, J. Shi, B. Tong, X. Feng, J. Zhi and Y. Dong, *Tetrahedron Lett.*, 2014, **55**, 1496–1500.